Phase retrieval from overexposed PSF

A projection-based approach

Soloviev, Oleg; Noom, Jacques; Nguyen, Hieu Thao; Vdovin, Gleb; Verhaegen, Michel

Citation (APA)
Soloviev, O., Noom, J., Nguyen, H. T., Vdovin, G., & Verhaegen, M. (2022). Phase retrieval from overexposed PSF: A projection-based approach. In Y. Liu, G. Popescu, & Y. Park (Eds.), *Quantitative Phase Imaging VIII* Article 119700K (Progress in Biomedical Optics and Imaging - Proceedings of SPIE; Vol. 11970). SPIE. https://doi.org/10.1117/12.2609697

Important note
To cite this publication, please use the final published version (if applicable).
Please check the document version above.

PROCEEDINGS OF SPIE

Phase retrieval from overexposed PSF: a projection-based approach

Soloviev, Oleg, Noom, Jacques, Nguyen, Hieu Thao, Vdovin, Gleb, Verhaegen, Michel

SPIE.

Phase retrieval from overexposed PSF: a projection-based approach

Oleg Soloviev[a,b], Jacques Noom[a], Nguyen Hieu Thao[a], Gleb Vdovin[a,b], and Michel Verhaegen[a]

[a]DCSC, TU Delft,Mekelweg 2, 2624 CD Delft, the Netherlands
[b]Flexible Optical BV, Polakweg 10–11, 2288 GG Rijswijk, the Netherlands

ABSTRACT

We investigate the general adjustment of projection-based phase retrieval algorithms for use with saturated data. In the phase retrieval problem, model fidelity of experimental data containing a non-zero background level, fixed pattern noise, or overexposure, often presents a serious obstacle for standard algorithms. Recently, it was shown that overexposure can help to increase the signal-to-noise ratio in AI applications. We present our first results in exploring this direction in the phase retrieval problem, using as an example the Gerchberg-Saxton algorithm with simulated data. The proposed method can find application in microscopy, characterisation of precise optical instruments, and machine vision applications of Industry4.0.

Keywords: phase retrieval, projection-based methods, overexposure

1. INTRODUCTION

In optical applications, phase retrieval (PR) is a general technique to obtain the pupil phase aberration of a system from its PSF p:

$$\text{find } \phi \text{ s.t. } \left| \mathcal{F} \, a e^{\mathrm{i}\phi} \right|^2 = p, \tag{1}$$

where a and p denote correspondingly the aperture transmission and the normalised light intensity in the focal plane, and $\mathcal{F}$ denotes the (2-dimensional) Fourier transform. PR finds use in the situations where introducing of a dedicated wavefront sensor is difficult or unwanted. A well known example is the detection of the mirror defect of the Hubble space telescope,[1] but it can also be applied for instance in characterisation of the objective aberration in semiconductor image-based quality tools.[2] Characterisation (and correction) of such aberrations is necessary to increase the inspection tool throughput required in Industry 4.0.[3,4]

A big class of PR methods is based on the projections.[5] In this approach, the phase retrieval problem is considered as a feasibility problem, that is finding a point x in the intersection of two sets A and B if such intersection is not empty, or point x of A closest to B in some sense, if such intersection does not exist:

$$\text{find } x \in A, \text{s.t. } \begin{cases} x \in B, & A \cap B \neq \emptyset, \\ x = \arg\min_{x \in A} d(x, B), & A \cap B = \emptyset, \end{cases} \tag{2}$$

for some distance metric d. In optical PR problem, variable x denotes a complex-valued two-dimensional function $x : \mathbb{R}^2 \mapsto \mathbb{C}$, and the sets A and B are defined as

$$A = \{|x| = a\}, \ B = \{|\mathcal{F} x|^2 = p\} \equiv \{|\mathcal{F} x| = \sqrt{p}\}, \tag{3}$$

where $\mathcal{F}$ denotes the (two-dimensional) Fourier transform. A projection-based method proceeds by iteratively updating estimates of x denoted as x^k using the projections of the previous estimates on sets A and B (more sophisticated combinations of the projections can provide better results[6]). The oldest method in the class—the Gerchberg-Saxton algorithm[7]—is just alternative projections on sets defined in (3):

$$x^{2k} = \Pr_A x^{2k-1}, \ x^{2k+1} = \Pr_B x^{2k}, \quad k \in \mathbb{N}. \tag{4}$$

Further author information: (Send correspondence to O.S.)
O.S..: E-mail: o.a.soloviev@tudelft.nl

In practice, the model defined by Eq. (1) does not hold for actual measurements of p. First of all, x, a, and p are substituted by sampled functions and are represented as arrays $x \in \mathbb{C}^{M \times N}$ and $a, p \in \mathbb{R}^{M \times N}$, and $\mathcal{F}$ denotes the two-dimensional DFT. Then combination of Equations (2) and (3) is assumed to be equivalent to (1). Besides the finite sampled representation, the model discrepancy may include quantization noise due to the final bit resolution of the imager, additive background signal, Gaussian noise of the detector, photon shot noise, and non-linear distortions of the signal like clipping which occurs as pixel saturation. Different techniques exist to mitigate the effects caused by the model discrepancy, which make the PR problem infeasible.[8] In this work, we focus on the saturation effect.

The saturation, or overexposure, might appear in astronomical applications[9] or in industrial adaptive optics application of laser beam quality optimisation.[10] In the latter, the aberration is corrected iteratively, the beam becomes more focused, and thus the peak intensity grows. The problem is usually solved by auto-exposure, that is adjusting the shutter time iteratively and discarding the saturated frames.

However, a recent work[11] has shown that overexposure can help deep-learning based PR methods and thus can be intentionally introduced as a preconditioner for more accurate phase estimation. This can be explained that although some information is lost in the overexposured areas, the SNR is improved in low-intensity regions. In addition, non-linear signal distortion is usually not a problem for the convolutional neural networks.

In this manuscript, we analyse the applicability of the projection-based methods to the single-image overexposured input data and show on example of numerical simulations that, with a corresponding redefinition of set B from Eq. (3), the overexposure can be used as a preconditioner with all projection-based PR methods.

2. DESCRIPTION OF A NUMERICAL SIMULATION

The numerical simulation consists of two parts: realistic simulation of a PSF measured by an optical system with certain physical parameters (forward model) and solving the inverse problem of finding the phase.

2.1 Forward model

Registered with digital camera PSF represents finite, sampled, clipped quantized noisy measurements of the intensity of the field in the focal plane. For the numerical simulations of PSF, we have used standard "padded DFT"[12] method to compute the noiseless field in the focal plane sampled on a large array, with the padding and sampling parameters defined by the numerical aperture of the lens, the light wavelength, and pixel size of the camera. We have used one of the two test phases shown in Fig. 1. We normalised this "ideal" sampled PSF by its maximum to unit value. Using a mixture of mathematical and pseudocode notation, the array p_i representing "ideal" PSF is computed as

$$p_i = \mathtt{rescale}(\left|\mathcal{F}\, a\mathrm{e}^{\mathrm{i}\phi}\right|^2), \quad a, \phi \in \mathbb{R}^{M_{\max} \times N_{\max}}, \tag{5}$$

with $\mathtt{rescale}(A) = A/\mathtt{maximum}(A)$.

From this array we sequentially:

- cropped a smaller square array representing the region of interest (ROI) of the camera,

- multiplicatively scaled to imitate different exposure time,

- added Gaussian noise for the camera noise (the Poisson noise was not considered in this work),

- clipped to 1 to represent the saturation,

- and quantized the values according to the camera bit resolution.

Thus in pseudocode:

$$p_s = \mathtt{quantization}(\mathtt{addgauss}(\mathtt{crop}(p_i, M) * l_{\mathrm{sat}}, \sigma), l_q), \tag{6}$$

where $\mathtt{quantization}(A, l_q)$ returns array A discretized to l_q levels between 0 and 1, $\mathtt{addgauss}(A, \sigma)$ returns array A with added Gaussian noise of zero mean and standard deviation σ, and $\mathtt{crop}(A, M)$ returns central $M \times M$ part of array A.
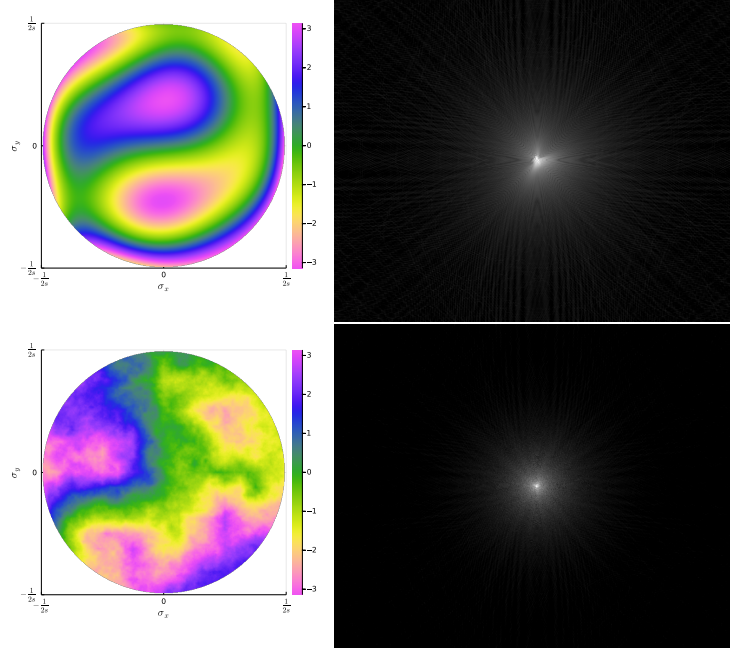
Figure 1. Two types of phases used in the simulations and the "ideal" PSFs p_i obtained from them: (top) low-order phase, (bottom) turbulent phase. The phases are shown wrapped, PSFs are shown in logarithmic scale for the values in the range $[2^{-24}, 1]$.
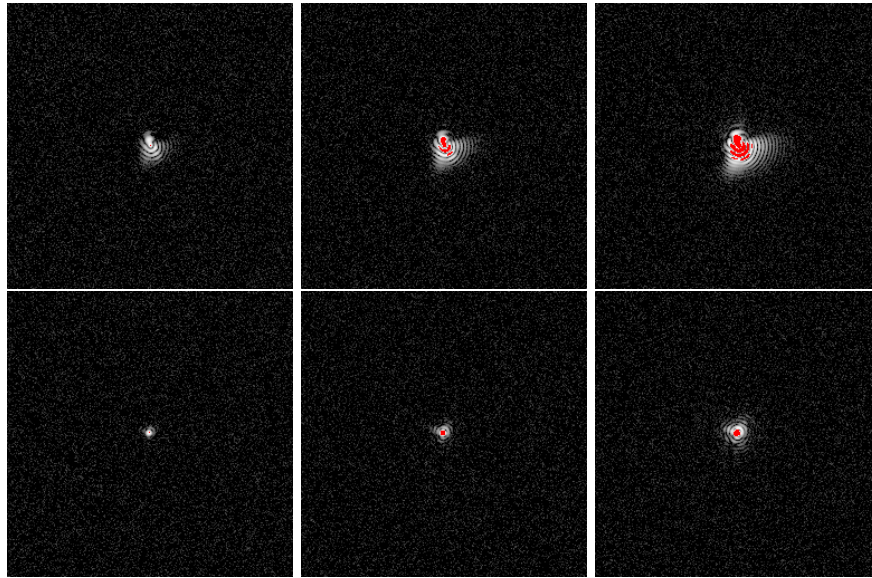

Figure 2. Input PSF with noise level $\sigma = 2/256$, saturation levels $l_{\text{sat}} = 0.95, 4, 16$ (left to right), registered with 8-bit quantisation, cropped to 256 pixels, for low-order (top row) and turbulent (bottom row) phases. Saturated PSF looses information in the centre but reveals more information in the side lobes. The saturated pixels are marked as red. PSF are shown in logarithmic scale in the range $[2^{-8}, 1]$.

We have fixed some imaging parameters corresponding to IDS camera UI-1540 (pixels size = 5.2 μm, sensor size 1280 × 1024, 8 bits per pixel) registering PSF formed by 1" lens with focal length 300 mm at 632 nm wavelength. In addition, we have 4 changing parameters describing the PSF as summarised in Table 1. The "ideal" PSFs p_i were calculated for the whole area of the imaging sensor; they are shown together with the phases used to produce them in Fig. 1. The saturated noisy PSFs were obtained as described above, several

examples are shown in Fig. 2.

<div align="center">

Table 1. Changing parameters for the PSF simulation

Parameter	Values
Phase type	"loworder", "turbulent", see Fig. 1
Noise level, σ	0, 2/256, 4/256
Crop size, M	128, 256, 512
Saturation level, l_{sat}	0.95, 2, 4, 8, 16

</div>

We see that the smoothness of the original phase affects the structure of the PSF and the effect of the overexposure. Thus, in PSF obtained from smooth low-order phase, the saturation results in a larger relative lost of data.

2.2 Inverse problem

The resulting array p_s for $l_{\text{sat}} <= 1$ (no saturation) for small values of noise is close to the original PSF p defined by Eq. (1) (up to some scaling factor), with arrays a and ϕ redefined to the crop size $M \times M$, but not equal to it (due to the nature of DFT, see reference 8 for details). For large enough crops we can however consider them close and search for the solution of the sampled problem:

$$\text{find } \phi \in \mathbb{R}^{M \times M} \text{ s.t. } \left|\mathcal{F}\,a\mathrm{e}^{\mathrm{i}\phi}\right|^2 \propto p_s, \tag{7}$$

where M is the crop size, and $\mathcal{F}$ stands for the two-dimensional DFT. Note that both normalisation scaling coefficient of the ideal PSF and saturation scaling l_{sat} are hidden here by replacing the equality to proportionality.

For $l_{\text{sat}} > 1$, the clipping introduced in the forward model changes the corresponding inverse problem:

$$\text{find } \phi \in \mathbb{R}^{M \times M} \text{ s.t. } \min\{l_{\text{sat}}\left|\mathcal{F}\,a\mathrm{e}^{\mathrm{i}\phi}\right|^2, 1\} \propto p_s \text{ for some } l_{\text{sat}} \in \mathbb{R}, l_{\text{sat}} \geq 1. \tag{8}$$

Note that here we cannot discard l_{sat} due to non-linearity of $\min\{\cdot, 1\}$ function.

2.3 Solving unsaturated inverse problem with projection-based algorithms

To solve the inverse problem defined by Eq. (1), we recalculate the binary array representing the aperture according to the crop size of the PSF. We define the input arrays a as this aperture and p_s as the input PSF. And we define $b = \sqrt{p_s}$, $x^0 = a$. Then, we proceed with the Gerchberg-Saxton (GS) algorithm summarised as follows:

$$x^{2k} = a \cdot \arg x^{2k-1}, \; x^{2k+1} = \mathcal{F}^{-1}(b \cdot \arg \mathcal{F}(x^{2k})), \quad k \in \mathbb{N}, \tag{9}$$

where arg and multiplication are taken element-wise and $\mathcal{F}$ denotes two-dimensional DFT. The stopping criteria for the algorithm are: exceeding the maximum number of iterations $k > k_{\max}$ or reaching convergence $\left\|x^{2k+2} - x^{2k}\right\| \leq \epsilon_{\text{tol}}$.

It is easy to see that the algorithm has the form of combined Eqs. (3, 4). We can also see that if the convergence is achieved at some step $2k'$ and $\left\|x^{2k'-1} - x^{2k'}\right\|$ is also small, the algorithm returns $x = x^{2k'}$ such that

$$|x| = a, \; |\mathcal{F}\,x|^2 \approx b^2 = p_s, \tag{10}$$
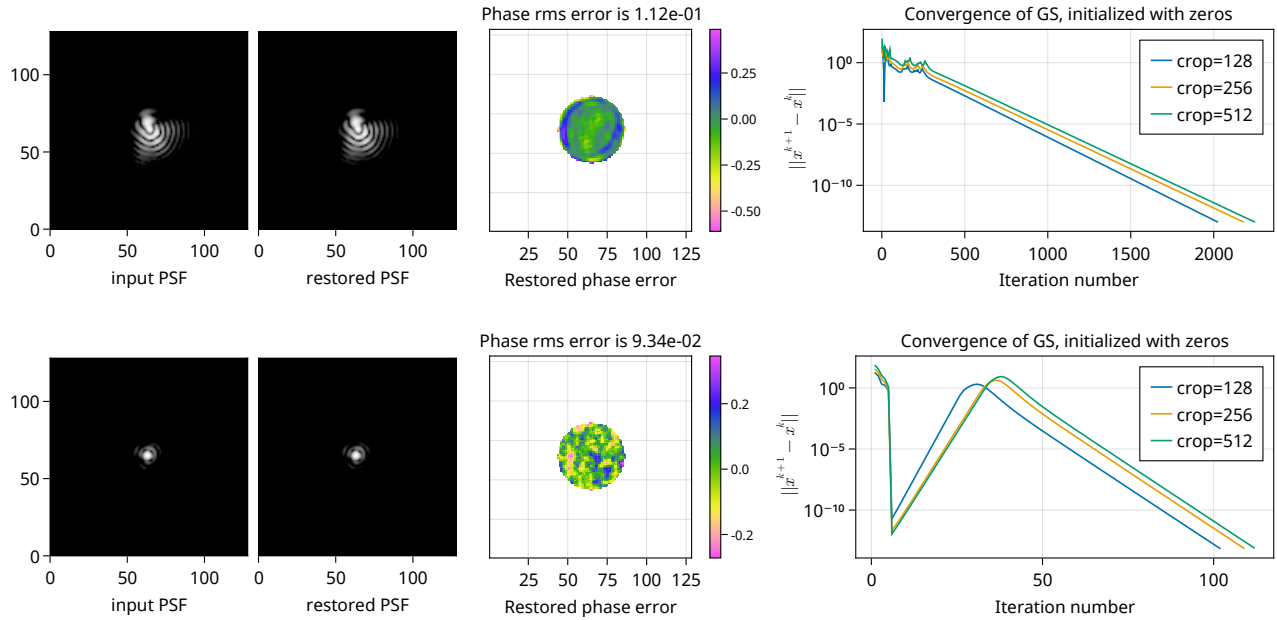
that is a solution of Eq. (7).

Figure 3. Example of input PSF (noiseless, quantised, unsaturated, crop size 128 pixels) and results of the GS algorithm ($\epsilon_{\text{tol}} = 10^{-13}$, $k_{\max} = 5000$ iterations): reconstructed PSF, reconstructed phase error, and the convergence plot for different crop sizes.

2.4 Establishing baseline: Performance of GS on unsaturated data

To illustrate the GS algorithm performance and establish a baseline for the performance comparison, we have run the GS algorithm on noiseless unsaturated data (note that cropping and quantisation still make the problem infeasible). The results are shown in Fig. 3 (PSFs and phase error are shown for crop size of 128 pixles, other crop values have similar results). We see typical for the alternating projections behaviour: after some initial search for a point in A close enough to B, the solution converges at linear rate to some fixed point, which results in an accurate representation of the PSF, but differs in phase slightly from the ground truth phase.

However, presence of even small noise can ruin the convergence (see Fig. 4, top row). The problem is usually addressed by thresholding of the input PSF (Fig. 4, middle and bottom rows), but even in the best cases the phase error increases. This can be explained that although higher level of threshold alleviates the noise influence, it also removes important information contained in the side lobes of the PSF. One can see that the restored PSF tries to satisfy the imposed constraint to have zero intensity in the thresholded region. On the other hand, lower levels of threshold lead to noise print trough in the solution, especially visible in the higher frequencies, where the original SNR is low.

2.5 Performance of GS on saturated PSF

As we have seen in Fig. 2, overexposured PSF increases SNR in high frequencies at expense of loosing information in the saturated part (often corresponding to the lower frequencies). Direct application of the GS algorithm to the saturated PSF does not provide a good solution, because the algorithm honestly tries to find the phase which produces the saturated PSF, and not the actual PSF before clipping. As can be seen in Fig. 5, presence of the saturated pixels increases the phase error even in the noiseless case, and increasing the saturation level results in a bigger restoration error.

3. SATURATED PSF SET AND PROJECTION ON IT

For $l_{\text{sat}} > 1$, the inverse problem is given by Eq. (8), and clearly GS will not find the correct solution. To see this, it is enough to understand that the ground truth—the point x given by the actual phase ϕ—is not the fixed
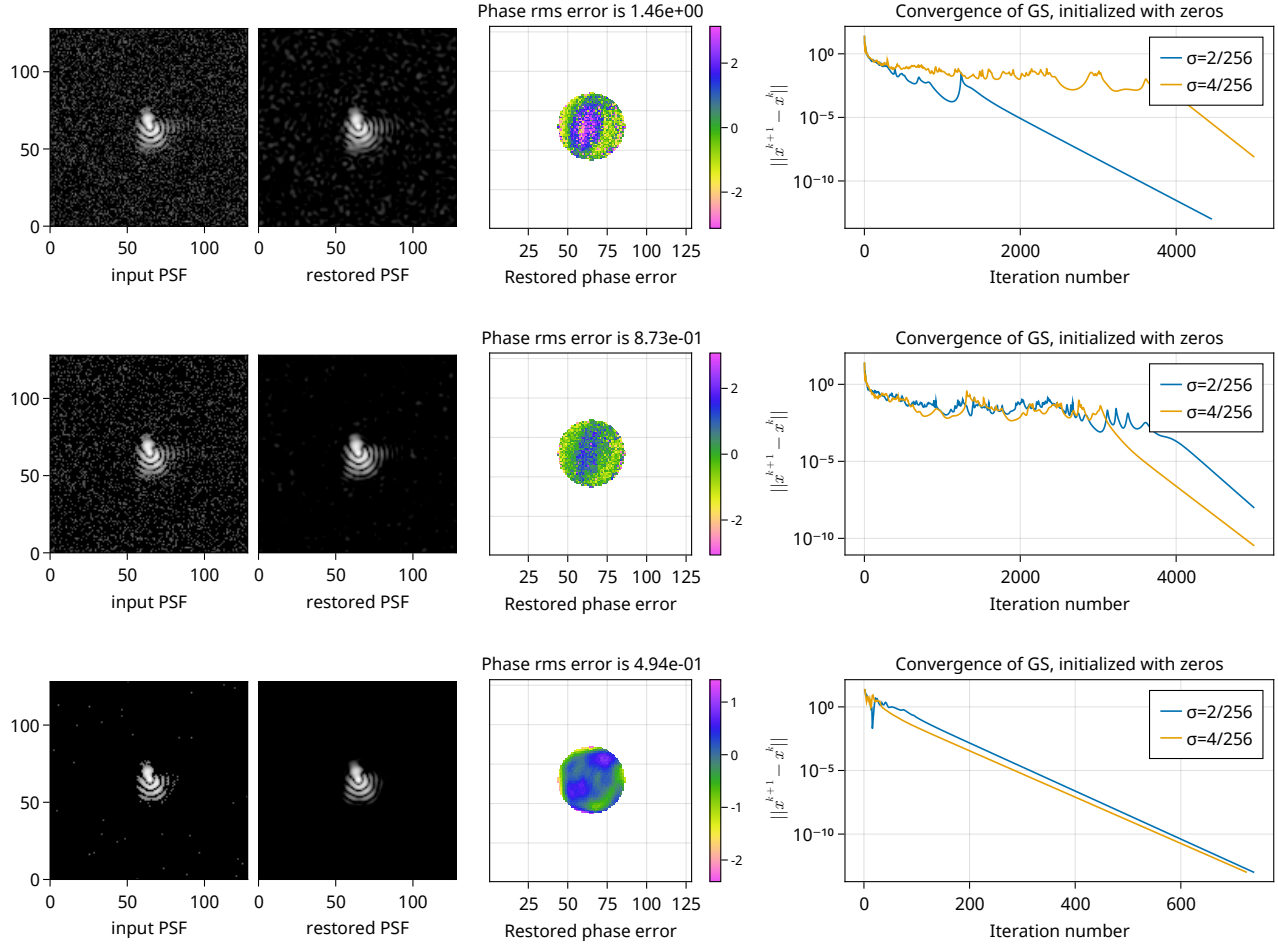
Figure 4. Example of thresholded noisy input PSF with threshold levels of $0, \sigma, 3\sigma$ (top to bottom) and results of the GS algorithm with the same parameters as in Fig. 3. The convergence plots for low threshold levels demonstrate random nature of the obtained results.

point of the algorithm (9). We need to replace the set B with some other set, for which the ground truth will be the fixed point.

For this, let us look for a modified GS algorithm in which the iteration still keep the phase, but the amplitude update rule is changed:

$$x^{2k} = a \cdot \arg x^{2k-1}, \ x^{2k+1} = \mathcal{F}^{-1}\left(h(|\mathcal{F} x^{2k}|) \cdot \arg \mathcal{F} x^{2k}\right), \quad k \in \mathbb{N}, \tag{11}$$

and let us try to define operator $h(\cdot)$ in form of projection on some set $\mathcal{H}$:

$$h(g) = \Pr_{\mathcal{H}} g \tag{12}$$

defined for all non-negative (sampled) functions $g(x)$.

Following the forward model (8), consider the class $\mathcal{H}_f$ of all functions, scaled clipped copy of which can be represented by a given real non-negative function $f(x), 0 \le f(x) \le 1$:

$$\mathcal{H}_f = \{h(x)| \ \exists s \in \mathbb{R}_+ : \min\{h(x), s\} = s \cdot f(x)\} \tag{13}$$

The idea behind it that the amplitude of the "real PSF", that is the Fourier transform of the ground truth, belongs to this set defined by $b = \sqrt{p_s}$:

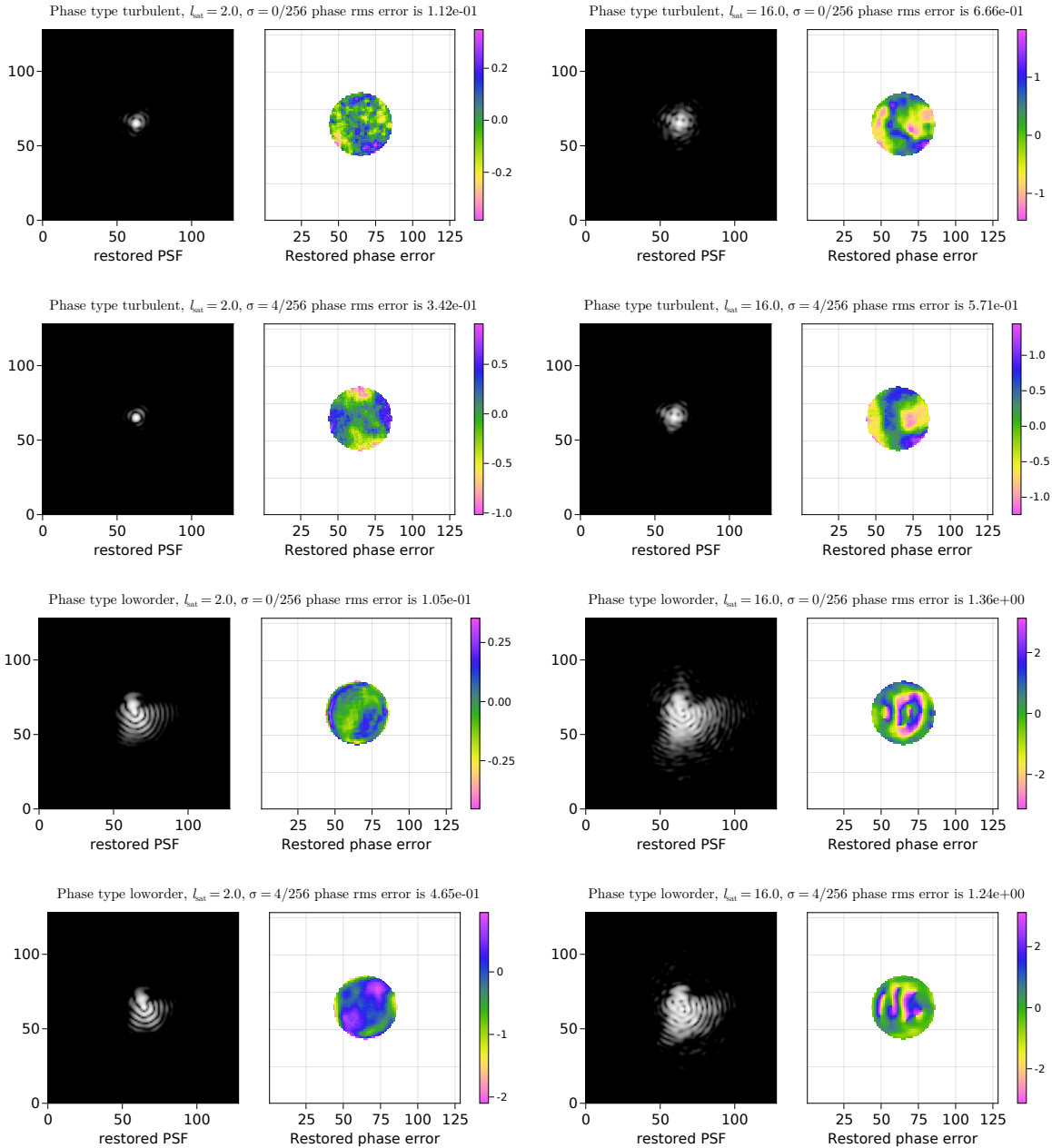$$\left|\mathcal{F} a \mathrm{e}^{\mathrm{i}\phi}\right| \in \mathcal{H}_b \tag{14}$$

Figure 5. PSFs and corresponding phase errors, restored with the GS algorithm from noiseless ($\sigma = 0$) and noisy saturated input. The input PSFs were thresholded at 3σ.

and thus the projection on this set does not change it: $\mathrm{Pr}_{\mathcal{H}_b} |\mathcal{F} x_{\mathrm{g.t.}}| = |\mathcal{F} x_{\mathrm{g.t.}}|$. Moreover, when updating the absolute value of the optical field in the focal plane, we will use the valid data from the unsaturated part "as is", just as GS does it, but in the saturated part, the projection may update the values or leave them "as is" if they are larger than the saturation level. The problem is complicated by the fact that the saturation level is not known, and we need to consider all possible values of it. See also Fig. 6 for an illustration.

Now let $g(x)$ be an arbitrary non-negative real function. We want to find the projection of g on $\mathcal{H}_f$. For this, let us define by "mask" all points where function f is saturated, that is $f = 1$. Denote values of functions f, g inside the mask as f_s, g_s. Denote by f_u, g_u the values of the functions in the unsaturated part, and let s_0 be
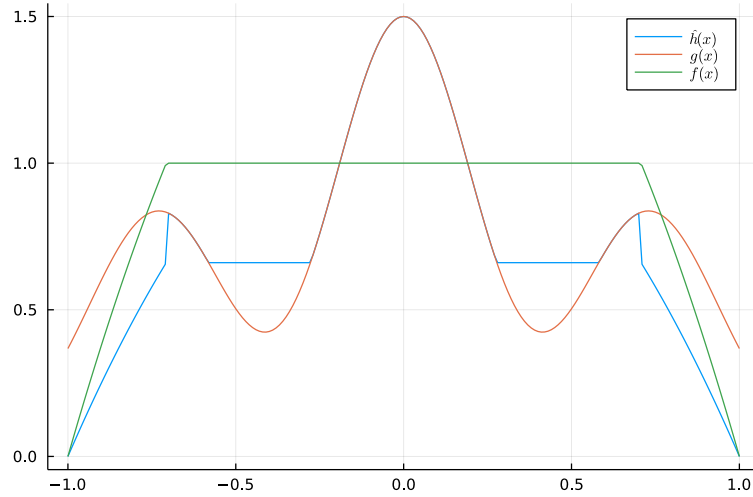
Figure 6. Illustrative example of projection on the "Saturated PSF set". Here f represents some clipped function (saturated PSF), and g is projected on the set of all functions, which can be clipped at some level and give a scaled version of f: $\exists s: \min\{\hat{h}(x), s\} = s \cdot f(x)$. In this example $\hat{h}$ is the closest in the least-squares sense to g of all such functions: if clipped at $\hat{s} \approx 0.66$, it has the same shape as f, and there is no closer to g function with such property.

the best scaling coefficient for these two vectors:

$$s_0 = \arg\min_s ||g_u(x) - s f_u(x)||^2. \tag{15}$$

Now, the squared distance between $g(x)$ and any function $h(x) \in \mathcal{H}_f$ is given by sum of the squared norm in the saturated and unsaturated parts:

$$d(h) = ||g(x) - h(x)||^2 = ||g_u(x) - h_u(x)||^2 + ||g_s(x) - h_s(x)||^2.$$

In the unsaturated part we have (by definition of s_0, see Eq. (15))

$$||g_u(x) - h_u(x)||^2 = ||g_u(x) - s f_u(x)||^2 = ||g_u(x) - s_0 f_u(x)||^2 + ||(s - s_0) f_u(x)||^2. \tag{16}$$

In the saturated part, function h may take any values greater than s, and thus we can chose such functions h that $h(x) = g(x)$ if $g(x) \geq s$, so the distance from g_s to $\mathcal{H}_f$ is defined only by the points x where $g(x) < s$, that is:

$$\min_{h \in \mathcal{H}} ||g_s(x) - h_s(x)||^2 = \sum_{i: g_s[i] < s} (g_s[i] - s)^2. \tag{17}$$

Thus $d(h)$ is calculated as sum of Eq. (16) and Eq. (17) and is completely characterised by value of saturation parameter s, $d(h) = r(s)$.

Function $r(s)$ is continuous smooth piece-wise quadratic function, and to minimise it, we can analyse its derivative $r'(s) = 2(s - s_0)||f_u||^2 + 2\sum_{i: g_s[i] < s}(s - g_s[i])$.

Without loss of generality, let g_s be monotone, $g_s[i] \leq g_s[j] \Leftrightarrow i \leq j$. Then $r'(s)$ is given a by linear interpolation between values in $g_s[i]$, and

$$r'(g_s[j]) = (g_s[j] - s_0)||f_u||^2 + \sum_{i<j}(g_s[j] - g_s[i]).$$

To find the root of such function is equivalent to find in the sorted sequence $r'(g_s[j])$ index j_0 of the last negative element and solve the linear equation $r'(s) = 0$ in the interval $s \in [g_s[j_0], g_s[j_0 + 1]]$.
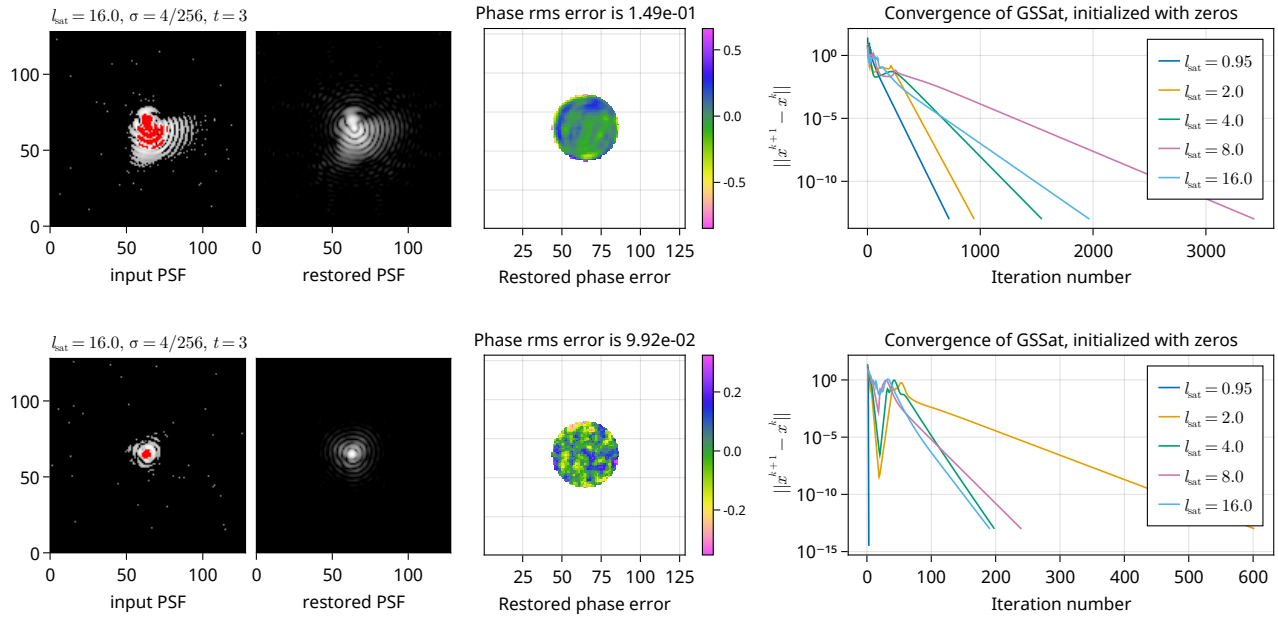
Figure 7. Performance of the proposed algorithm on saturated data for loworder (top) and turbulent (bottom) test phases. Noisy saturated PSFs were thresholded at 3σ, examples of the input and restored PSFs and the phase error are shown for saturation level $l_{\text{sat}} = 16$ and noise level $\sigma = 4/256$. Convergence plots are shown for changing levels of saturation.

The root $\hat{s}$ of this equation defines projection $\hat{h} = \text{Pr}_{\mathcal{H}_f}$ as

$$\hat{h}(x) = \begin{cases} \hat{s}f(x) & \text{if } f(x) < 1, \text{ (unsaturated part, valid data)}, \\ \max\{\hat{s}, g(x)\} & \text{if } f(x) = 1, \text{ (saturated part, invalid data)}. \end{cases} \tag{18}$$

Substituting this projection into Eq. (11), we obtain a modified GS algorithm (named here GSSat), able to work with the saturated PSF as its input.

4. RESULTS

Providing to the GSSat the same noisy saturated PSFs as in Fig. 5, we were able to restore the phase with an accuracy comparable with that of the standard GS method on the noiseless input (compare Fig. 7 and Fig. 3). Note the convergence behaviour is again typical for a stable solution.

Figure 8 gives an overview of the GSSat performance depending on the saturation level. From it it is clear that higher saturation levels indeed act as preconditioner and improve the accuracy of the retrieved phase.

5. DISCUSSION AND CONCLUSION

We have proposed and demonstrated on example of the Gerchberg-Saxton algorithm a modification of a general projection-based phase retrieval method which allows to use a saturated PSF as its input. Due to increased SNR in the side lobes of the overexposured PSF and the ability of the algorithm to reconstruct the lost data in the saturated area, the algorithm retrieves the phase with the accuracy comparable to that of the standard algorithm on a noiseless data. The algorithm can be used, for instance, in industrial applications, where it is either difficult to obtain PSF without overexposure or with a good SNR.
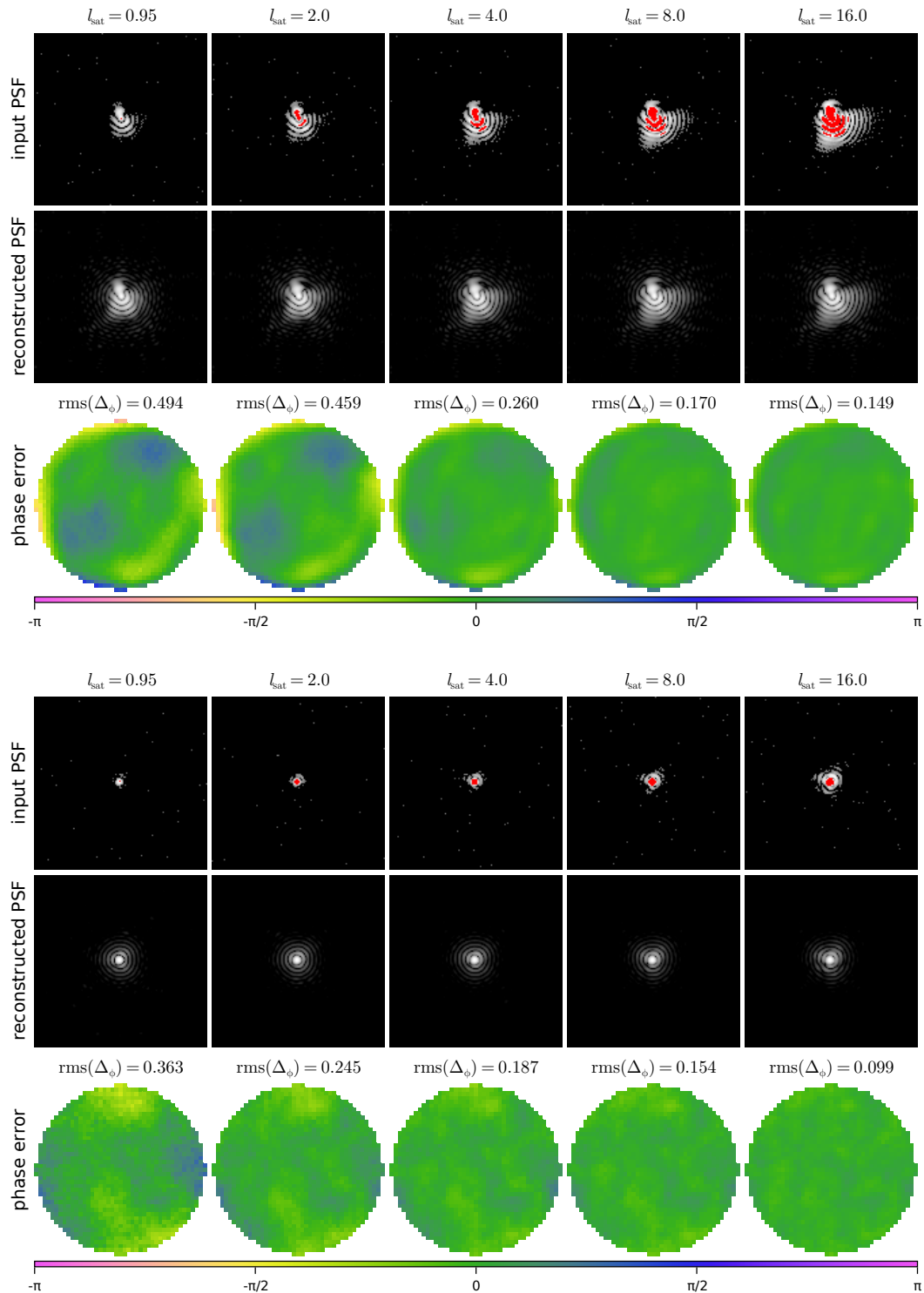
Funding

Figure 8. Overview of the performance of the GSSat on noisy thresholded saturated input for different levels of saturation for loworder (top) and turbulent phases. All input PSF had noise level of $\sigma = 4/256$, thresholded at 3σ, crop size $M = 128$.

REFERENCES

[1] Fienup, J. R., Marron, J. C., Schulz, T. J., and Seldin, J. H., "Hubble Space Telescope characterized by using phase-retrieval algorithms," *Appl. Opt.* **32**, 1747 (apr 1993).

[2] Ansuinelli, P., Coene, W., and Urbach, P., "EUV mask feature reconstruction via phase retrieval," (September 2019), 88 (2019).

[3] Beckert, E., Kyriakoulis, N., Milenkovic, J., Tsolekas, V., Mantelos, A., and Chondronasios, A., "Multi-sensor and closed-loop control of component and assembly processes for zero-defect manufacturing of photonics," in [*Smart Photonic Optoelectron. Integr. Circuits XXII*], He, S. and Vivien, L., eds., 12, SPIE (feb 2020).

[4] Coffey, V. C., "Machine Vision: The Eyes of Industry 40," *Opt. Photonics News* **29**, 42 (jul 2018).

[5] Marchesini, S., "A unified evaluation of iterative projection algorithms for phase retrieval," *Rev. Sci. Instrum.* **78**(1) (2007).

[6] Thao, N. H., Soloviev, O., and Verhaegen, M., "Convex combination of alternating projection and Douglas–Rachford operators for phase retrieval," *Adv. Comput. Math.* **47**, 33 (jun 2021).

[7] Gerchberg, R. W., "A practical algorithm for the determination of phase from image and diffraction plane pictures," *Optik* **35**, 237–246 (1972).

[8] Luke, D. R., "Phase Retrieval, What's New?," *SIAG/OPT Views News* **25**(1), 1–6 (2017).

[9] Hirsch, M., Harmeling, S., Sra, S., and Schölkopf, B., "Online multi-frame blind deconvolution with super-resolution and saturation correction," *Astron. Astrophys.* **531**, A9 (jul 2011).

[10] Patlan, V., Soloviev, O., and Vdovin, G. V., "Optimal diffraction-limited focusing through static aberrations," in [*Proc. SPIE - Int. Soc. Opt. Eng.*], Forbes, A. and Lizotte, T. E., eds., **9194**, 91940E, SPIE (sep 2014).

[11] Nishizaki, Y., Valdivia, M., Horisaki, R., Kitaguchi, K., Saito, M., Tanida, J., and Vera, E., "Deep learning wavefront sensing," *Opt. Express* **27**, 240 (jan 2019).

[12] Jurling, A. S., Bergkoetter, M. D., and Fienup, J. R., "Techniques for arbitrary sampling in two-dimensional Fourier transforms," *J. Opt. Soc. Am. A* **35**, 1784 (nov 2018).